nature nanotechnology

Letter

https://doi.org/10.1038/s41565-022-01224-y

Lorentz electron ptychography for imaging magnetic textures beyond the diffraction limit

Received: 9 November 2021

Accepted: 5 September 2022

Published online: 31 October 2022

Check for updates

Zhen Chen[1,2] ✉, Emrah Turgut[3], Yi Jiang[4], Kayla X. Nguyen[5], Matthew J. Stolt[6], Song Jin[6], Daniel C. Ralph[7,8], Gregory D. Fuchs[1] and David A. Muller[1,8] ✉

Nanoscale spin textures, especially magnetic skyrmions, have attracted intense interest as candidate high-density and power-efficient information carriers for spintronic devices[1,2]. Facilitating a deeper understanding of sub-hundred-nanometre to atomic-scale spin textures requires more advanced magnetic imaging techniques[3–5]. Here we demonstrate a Lorentz electron ptychography method that can enable high-resolution, high-sensitivity magnetic field imaging for widely available electron microscopes. The resolution of Lorentz electron ptychography is not limited by the usual diffraction limit of lens optics, but instead is determined by the maximum scattering angle at which a statistically meaningful dose can still be recorded—this can be an improvement of up to 2–6 times depending on the allowable dose. Using FeGe as the model system, we realize a more accurate magnetic field measurement of skyrmions with an improved spatial resolution and sensitivity by also correcting the probe-damping effect from the imaging optics via Lorentz electron ptychography. This allows us to directly resolve subtle internal structures of magnetic skyrmions near the skyrmion cores, boundaries and dislocations in an FeGe single crystal. Our study establishes a quantitative, high-resolution magnetic microscopy technique that can reveal nanoscale spin textures, especially magnetization discontinuities and topological defects in nanomagnets[6]. The technique's high-dose efficiency should also make it well suited for the exploration of magnetic textures in electron radiation-sensitive materials such as organic or molecular magnets[7].

Magnetic skyrmions are non-collinear, swirling or hedgehog-like spin solitons with an integer topological index[8]. Since their discovery[9], magnetic skyrmions have been observed by either neutron diffraction[9] or real-space imaging techniques[3–5]. Real-space imaging techniques with a high spatial resolution play crucial roles in the studies of skyrmions, especially when disorder[3] or deformation[10] of skyrmions occur. Commonly used magnetic imaging methods such as magnetic force microscopy (MFM) or X-ray microscopy have resolution limits of about

[1]School of Applied and Engineering Physics, Cornell University, Ithaca, NY, USA. [2]School of Materials Science and Engineering, Tsinghua University, Beijing, China. [3]Department of Physics, Oklahoma State University, Stillwater, OK, USA. [4]Advanced Photon Source, Argonne National Laboratory, Lemont, IL, USA. [5]Department of Chemistry and Chemical Biology, Cornell University, Ithaca, NY, USA. [6]Department of Chemistry, University of Wisconsin–Madison, Madison, WI, USA. [7]Department of Physics, Cornell University, Ithaca, NY, USA. [8]Kavli Institute at Cornell for Nanoscale Science, Ithaca, NY, USA. ✉e-mail: zhenchen01@tsinghua.edu.cn; david.a.muller@cornell.edu

https://doi.org/10.1038/s41565-022-01224-y

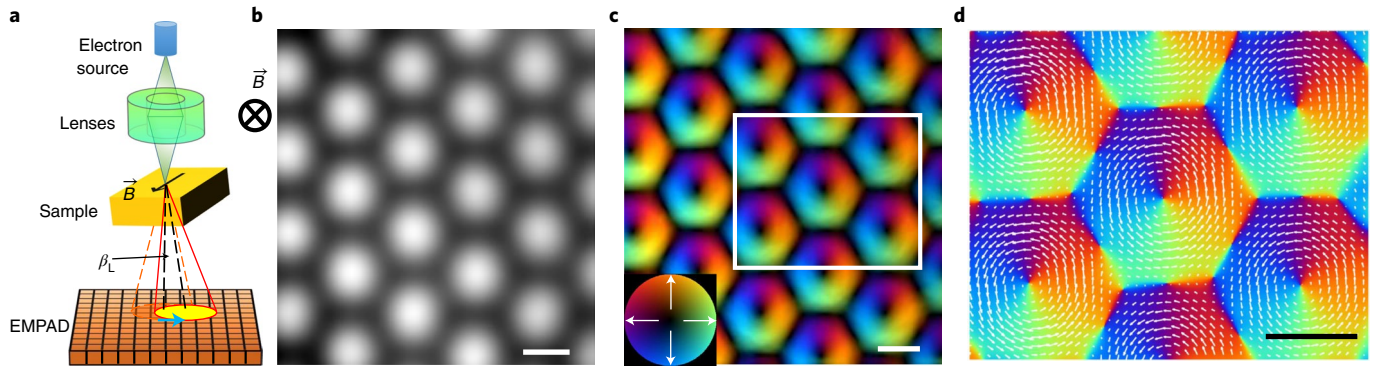

Fig. 1 | Workflow for LEP. a, The 4D-LSTEM setup. The deflection angle β_L caused by the lateral magnetic induction field (**B**) in the sample via the Lorentz force is measured by a 2D pixel array detector, such as an EMPAD. **b**, Measured magnetic phase shift of a skyrmion lattice in FeGe reconstructed from LEP using a 4D-LSTEM dataset. Out-of-plane component of **B** goes inwards (labelled as a circle with a cross). **c**, Lateral magnetic field map calculated via the first-order gradient of the phase recorded in **b**. The colour shows the direction, and the brightness shows the magnitude, as given by the colour wheel in the lower left inset in **c**. **d**, Magnetic-field vector map from the enlarged region marked by a white box in **c**. The arrows represent the magnetic field vectors with the length representing the lateral magnetic field magnitude. The false colour shows only the magnetization direction. The dataset was acquired at a temperature of 94 K with an external magnetic field of 130 mT pointing into the page. Scale bars, 50 nm.

10–20 nm (refs. [4,11,12]). Scanning tunnelling microscopy techniques can provide a sub-nanometre resolution[13], but they are more surface sensitive and incapable of revealing the full internal structure of magnetic skyrmions. Higher-resolution methods based on Lorentz electron microscopy, such as Lorentz transmission electron microscopy (LTEM) or electron holography can, in principle, reach resolutions below 10 nm and provide sensitivity to bulk-like structures up to a depth of almost a micrometre[5]. However, these electron microscopy methods have limitations, either in resolution due to delocalization effects from the defocused illumination in LTEM[14] or in sensitivity from the limited electron doses that can be applied due to the coherent source requirements for electron holography[15].

As an alternative, differential phase-contrast (DPC) imaging directly measures the local magnetic field using focused-probe illumination in the Lorentz scanning transmission electron microscopy (LSTEM) geometry. However, the resolution is limited by the probe size and the signal-to-noise ratio (SNR) determined by the saturation dose rate of the detector. Probe sizes of a few nanometres down to the sub-nanometre scale[16] have been recently demonstrated, limited by the aberrations of the lens optics in magnetic-field-free conditions that are usually required for magnetic imaging. However, achieving both high resolution and high SNR with DPC requires the use of a tiny, non-distorted probe and a high-dynamic-range detector capable of acquiring high-dose illumination, which is an extremely challenging combination.

Figure 1a shows a schematic of the experimental setup for acquiring the four-dimensional LSTEM (4D-LSTEM) datasets used in Lorentz electron ptychography (LEP). The four-dimensional (4D) datasets are formed by acquiring the full diffraction pattern at each probe position as a focused probe is scanned with a few nanometres in diameter across the sample utilizing a high-dynamic-range electron microscope pixel array detector (EMPAD)[17]. Different from conventional 4D scanning transmission electron microscopy[18], a major challenge for 4D-LSTEM is that the main image-forming lens (objective lens) of the microscope is used to set the external magnetic field at the sample; therefore, beam focusing is accomplished using a more distant lens. This allows imaging with control over the external field condition at the sample, including the option of a magnetic-field-free condition that may be necessary to preserve the intrinsic magnetic structures. The much longer focal length of the substitute lens results in larger aberrations and can limit the probe size to a few nanometres, thus lowering the spatial resolution of 4D-LSTEM. Instead of using a standard probe deflection method for image recovery such as DPC, we employ an iterative phase-retrieval approach by LEP and reach a spatial resolution beyond the probe-size limit.

The imaging mode of 4D-LSTEM can be qualitatively understood from classical electromagnetism: fast electrons are deflected by the lateral magnetic induction field $\mathbf{B}(\mathbf{x}, \mathbf{y})$ in the sample via the Lorentz force. The deflection angle β_L is linearly proportional to the field[19], that is, $\beta_L = e^- Bt\lambda/h$, where e^- is the charge of an electron, t is the sample thickness, λ is the wavelength of electrons and h is the Planck constant. From the 4D datasets, the expectation value for the deflection angle can be determined from the measured diffraction patterns by calculating the centre of mass (CoM) in the x–y plane of the detector, providing what is, in effect, a more accurate analogue of DPC. One example is shown in Extended Data Fig. 1b,c. Meanwhile, the 4D datasets also contain crystalline structure information of the samples, such as the crystalline morphologies obtainable by synthetically forming scanning transmission electron microscopy images such as annular dark-field images (Extended Data Fig. 1a). This can be especially useful in polycrystalline samples for disentangling the crystal structure contribution from the magnetic fields[20]. The sample thickness (Extended Data Fig. 1d), which is important for quantifying the magnetic field, can also be determined from the diffraction patterns (Methods).

In a more quantitative quantum-mechanical treatment, the complex wavefunction of the electron probe travelling along the optic axis (z axis) through a sample with a projected magnetic vector potential $A_z(x, y)$ acquires a phase shift $\varphi_m(x, y)$ via the Aharonov–Bohm effect[21], as discussed in the literature in the context of LTEM[14] and electron holography[5,19]. This phase shift can be retrieved either via a transport-of-intensity equation approach using focal-series LTEM images or from the shift in interference fringes in electron holography. The in-plane $\mathbf{B}(x, y)$ field can then be directly calculated from a first-order gradient of the phase[5]. In general, the electrostatic potential $\varphi_e(x, y)$ of the sample also contributes to the total phase shift and must be accounted for (Methods).

Here we demonstrate that the phase shift can also be obtained from 4D electron diffraction measurements via a computational phase-retrieval method, namely, LEP. This approach is well suited for correcting the aberration-induced image distortions from the optics and achieves an enhanced SNR, improved resolution and higher accuracy for quantitative magnetic field measurement. Figure 1b shows the phase shift experimentally reconstructed via LEP showing a skyrmion lattice state in a single crystal of FeGe at 94 K after cooling from 240 K in an external magnetic field of $\mu_0 H = 130$ mT. Figure 1c shows the lateral

https://doi.org/10.1038/s41565-022-01224-y

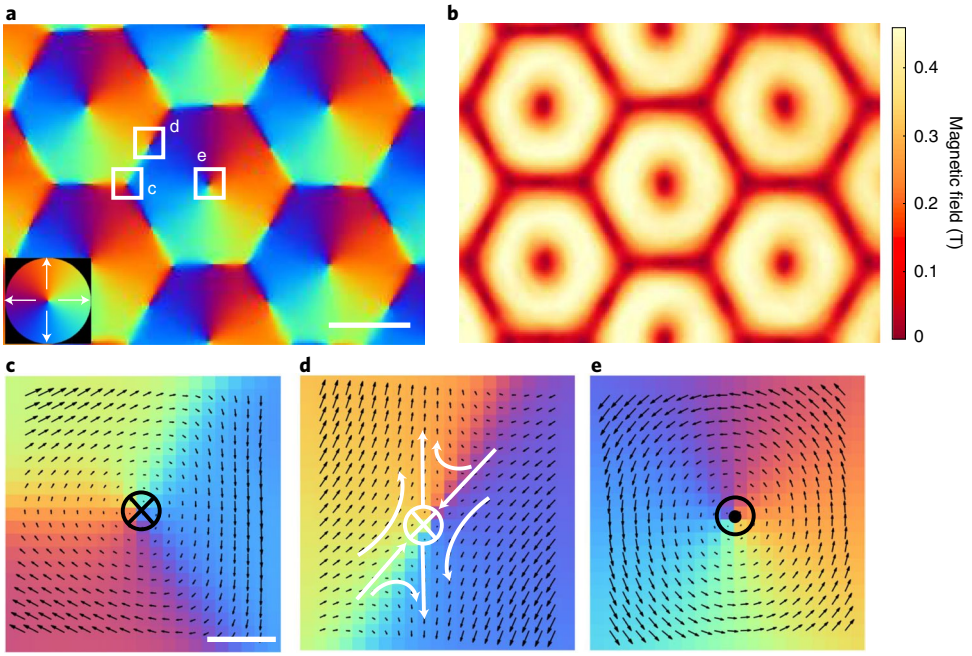

Fig. 2 | Measured lateral magnetic induction field of a skyrmion lattice in FeGe. a,**b**, Direction (**a**) and magnitude (**b**) of the lateral magnetic field obtained by LEP. Scale bar, 50 nm. **c**–**e**. Magnetic field near a skyrmion corner (**c**), boundary (**d**) and core (**e**) from the positions marked in **a**, showing the in-plane singularities. Scale bar, 2 nm. A schematic showing the lateral magnetization around the anti-vortex point is overlaid in **d**. The black arrows in **c**–**e** show the magnetic vectors with length representing the lateral magnitude. The out-of-plane component of the magnetic field is outwards near the skyrmion cores and inwards near the boundaries, labelled as a circle with a cross in **c** and a circle with a dot in **e**, respectively.

vector field $\mathbf{B}(x, y)$ of the skyrmion lattice directly obtained from the gradient of the phase shown in Fig. 1b. FeGe is a good model system as the skyrmion lattices in FeGe single crystals have been imaged using different electron microscopy methods, such as LTEM[22], electron holography[23] or DPC imaging[24], but the internal spin structure was barely resolved due to the limited SNR, even though detailed simulations of this internal structure have been made[23]. To show the details of the field distribution, the boxed region in Fig. 1c is enlarged in Fig. 1d, with the field vectors displayed as arrows. The counterclockwise swirling magnetic structure of the Bloch-type skyrmions can be directly seen.

More importantly, the internal structures of the skyrmion lattice are easily identified from the field direction map shown in Fig. 2a, including singular points like the vortex cores and sharp boundaries between skyrmions. Several singular points are highlighted in Fig. 2c–e. Figure 2e directly shows the counterclockwise swirling approaching the inner core of skyrmions. The shared corner of three neighbouring skyrmions shows a reversed vortex, that is, clockwise (Fig. 2c). Additionally, the lateral spin structure at the midpoint of the boundaries between two skyrmions has an anti-vortex-like texture (Fig. 2d). It is expected that at singular points, the direction of the lateral component of magnetization in the x–y plane abruptly changes and the magnitude approaches zero[25]. Therefore, a high SNR together with a small measurement uncertainty is needed for imaging the magnetization near the singular points, and it is these details that have not been revealed by previous experimental measurements[23,24]. The high precision of our LEP results can be illustrated from vector field images (Fig. 2c–e), as the magnetic vector direction at one pixel away from the singular points, ~1.2 nm, is still well defined, even though the magnitude of the lateral field is smaller than 20 mT. The discontinuities in the lateral magnetization vector field can be more clearly seen in the line profiles across the singular points (Extended Data Fig. 2). Interestingly, along a boundary between skyrmions, there are two local maxima in the magnitude of the magnetic field along the skyrmion boundary (marked by arrows in Extended Data Fig. 2e, inset). These are formed due to the two-dimensional (2D) anti-vortex structure (Fig. 2d), which has been discussed in the context of simulations[24] and electron holography[23].

It is not surprising that the projected lateral field contains 2D singularity points at the vortex cores and skyrmion boundaries, even though skyrmions are smooth topological objects in three-dimensional space that do not have singularities, that is, no vanishing of the 3D magnetization along points, lines or planes[8]. This was noted in previous simulations[23,24]. We can reproduce the 2D singularity points such as the reversed vortex and anti-vortex at the corners and boundaries of the skyrmion lattices via micromagnetic simulations (Extended Data Fig. 3). These projected 2D singularity points share a common topology with 2D spin systems[25]. In 2D, the winding number of vortex cores and reversed vortex cores at the corners is +1, whereas the anti-vortexes have a winding number of −1 (ref. [25]). The total winding number of a single 2D skyrmion in a lattice is 0, which is required for a 2D vector field according to the Poincaré–Hopf theorem[26].

LEP is also very effective at delineating changes in the internal spin structure to accommodate an edge dislocation in the skyrmion lattice (Fig. 3a). As skyrmions are quasiparticles, the edge dislocation shows a pentagon–heptagon membrane structure similar to crystalline edge dislocations. Sharp polygons and their boundaries can be more easily identified in the magnetization direction (Fig. 3b). Because skyrmions are also topologically protected and have very high flexibility, they can undergo substantial deformations. We observe that skyrmions near the dislocation core are notably distorted. The anisotropic factor for the heptagon is as large as ~22%, and the area of the heptagon is ~2.5 times that of the pentagon. However, the topology of magnetization winding at the dislocation core of the skyrmions is still conserved, the same as in perfect regions of the skyrmion lattice.

The improved precision and resolution of the LEP technique enables us to directly image spin structures near the singular points of skyrmion lattices with accurate measurements of the size and position of each skyrmions. A qualitative sense of the improved resolution for LEP can be seen from the sharp boundaries of the skyrmions

https://doi.org/10.1038/s41565-022-01224-y

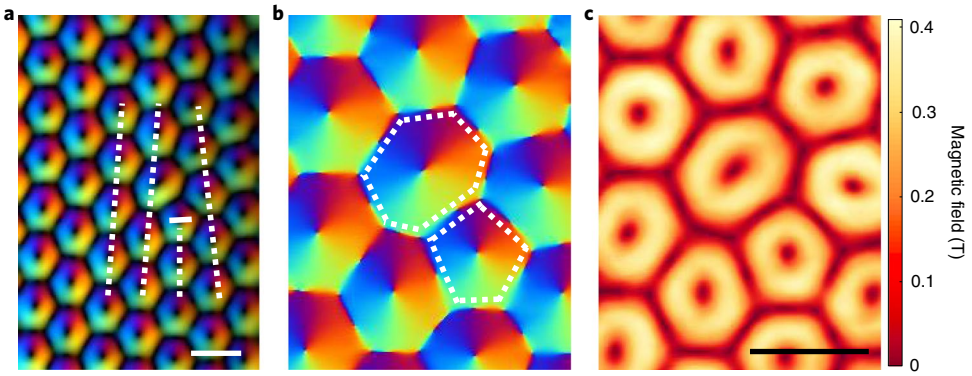

Fig. 3 | Skyrmion-lattice edge dislocation in FeGe. a, Lateral magnetization direction in a skyrmion lattice containing an edge dislocation. **b**,**c**, Zoomed-in lateral magnetization direction (**b**) and magnitude (**c**) near the dislocation core. The white dashed lines in **b** outline the 5–7 pairs near the dislocation core. The images were recorded at a temperature of 94 K and an external magnetic field: $\mu_0 H = 130$ mT for **a**; $\mu_0 H = 160$ mT for **b** and **c**. The lateral magnetic field in **a** is directly determined from the CoM of diffraction patterns and **b** and **c** are determined from ptychography. Scale bars, 100 nm.

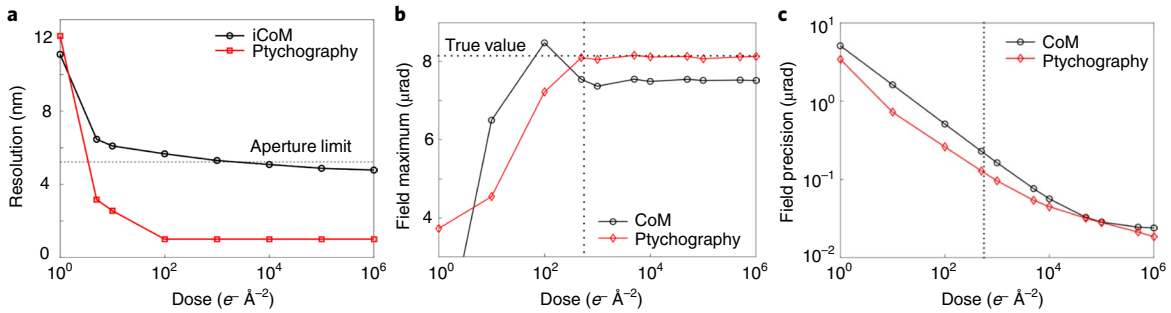

Fig. 4 | Quantification of field measurements from LEP. a, Resolution of field measurements from the diffraction-limited, direct iCoM analysis and ptychography as a function of illumination dose. **b**,**c**, Field maximum and field precision for direct CoM and ptychography. The simulations in **a** used a model field distribution with peak features of varying distances (Extended Data Fig. 5d) to capture a wide frequency range, and **b** and **c** used the model field distribution shown in Extended Data Fig. 6a, intended to match the skyrmion lattice in the experiments.

(Figs. 2a and 3b and the enhancement in the peak field compared with that from the CoM (Extended Data Fig. 4)). However, determining the spatial resolution is not straightforward, because the feature size of the magnetic textures is much larger than the probe size and thus any expected resolution estimate. As with conventional ptychography, the resolution is dependent on the illuminating dose[27]. Figure 4a shows the dose-dependent resolution estimated from simulations by using a model structure with peaks of varying distances to ensure a wide range of Fourier coefficients (Extended Data Fig. 5 and Methods). Sub-nanometre resolution is achievable at doses higher than 100 e^- Å^{-2} and probe size of 5.2 nm, both of which are similar to that used for our experiments. Therefore, it has the potential to be 2–6 times better in resolution than the diffraction limit of the probe-forming aperture.

The phase precision for LEP estimated from the local fluctuation in terms of standard deviation (σ) is determined to be 2 ± 1 mrad or $2\pi/3{,}142$ rad for the experimental data shown in Fig. 2 (Methods). This measurement uncertainty is extracted from a 60-nm-thick sample region, rather than the best-case free-space scenario. Therefore, it should be considered as a conservative upper limit, because the intrinsic fluctuation of the field in the sample, such as from surface roughness, also contributes to this variation. In contrast, the best reported phase precision from electron holography is typically $2\pi/1{,}500$ rad, measured in vacuum (where fringe contrast is the highest) after an extensive image integration[28], and typical recent results are around $2\pi/1{,}150$ rad (ref. [29]). Therefore, the precision achieved by LEP is at least a factor of two to three beyond what has been demonstrated by electron holography. We note that this improvement is similar to the reported 3.75 times improvement in DPC in the high-dose limit compared with electron holography on the same sample region[29]. At lower doses, we would expect an improvement of a factor of two for LEP over DPC (Fig. 4c). The corresponding precision for magnetic field measurements is provided in the Methods section.

LEP allows for highly accurate magnetic field measurements since the effects of distortion and damping of the probe beam can be corrected. In contrast, what CoM or DPC measures is the field convolved with the incident probe function that inevitably introduces damping and distortion. As shown in Fig. 4b, from simulations using a model phase distribution (Extended Data Fig. 6a), LEP can measure the field magnitude (for example, maximum) very accurately when the illuminating dose is higher than 500 e^- Å^{-2}, whereas the field maximum from CoM, in comparison, is more than 10% reduced due to the probe convolution effect. The probe-damping effect can be reduced by a deconvolution procedure[30] in cases where the probe shape is known, but this is not always possible, especially for sub-nanometre and atomic-resolution imaging conditions. The improvement becomes increasingly substantial for increasingly sub-nanometre resolution. Further, the precision of field measurements using LEP is two times better than CoM for the same illumination dose (Fig. 4c).

Another advantage of the LEP technique is its high-dose efficiency. As shown in Extended Data Fig. 6c–f, LEP with a dose as low as 1–10 e^- Å^{-2} still shows clear sub-ten-nanometre features in the phase and field images. Such low doses are tolerable even for many electron-beam radiation-sensitive organic molecules[31]. Therefore, LEP is well suited to study the spin textures in a wide range of organic or molecular magnets[7], which have potential applications in next-generation spintronic devices[7] but remain largely unexplored due to the lack of suitable real-space imaging tools.

The limiting factors for the precision improvement of LEP include the degree of probe coherence especially for large beam current conditions and the surface roughness of the specimen. The surface roughness of the sample introduces fluctuations due to electrostatic potential contributions. It can be removed by subtracting uniform magnetic states (for example, above the Curie temperature or magnetic saturation state) or reversed magnetic states from the same sample region, which has been similarly adapted in electron holography[5]. A high-coherence probe is also preferred for electron ptychography, because for a fixed maximum allowable dose, the SNR decreases with coherence. However, compared with electron holography, an advantage of the LEP technique is that the redundancy in information channels makes it possible to account for inevitable partial coherence of illumination using mixed-state ptychography algorithms[32]. Nevertheless, using a brighter and more coherent source, such as a cold field-emission gun, can further improve the measurement precision. Additionally, LEP can retrieve the mixed quantum states and three-dimensional magnetic structure information of the sample if more advanced algorithms are implemented[32,33].

In summary, we have demonstrated that the phase induced by the magnetic flux from skyrmions can be reconstructed from LEP. Utilizing this high-resolution and high-precision magnetic imaging technique, we directly revealed the details of the 2D magnetization singularities in a skyrmion lattice in FeGe with a nanometre-scale resolution. We quantitatively measured the saturation field and effects of skyrmion lattice dislocations in FeGe, which are crucial for a comprehensive description of skyrmion states. This real-space magnetic imaging technique provides a unique tool for investigating the topology, dynamics and singularities of different spin textures in many magnetic materials and spintronic devices.

Online content

Any methods, additional references, Nature Research reporting summaries, source data, extended data, supplementary information, acknowledgements, peer review information; details of author contributions and competing interests; and statements of data and code availability are available at https://doi.org/10.1038/s41565-022-01224-y.

References

1. Fert, A., Cros, V. & Sampaio, J. Skyrmions on the track. *Nat. Nanotechnol.* **8**, 152–156 (2013).
2. Mathur, N., Stolt, M. J. & Jin, S. Magnetic skyrmions in nanostructures of non-centrosymmetric materials. *APL Mater.* **7**, 120703 (2019).
3. Yu, X. Z. et al. Real-space observation of a two-dimensional skyrmion crystal. *Nature* **465**, 901–904 (2010).
4. Milde, P. et al. Unwinding of a skyrmion lattice by magnetic monopoles. *Science* **340**, 1076–1080 (2013).
5. Park, H. S. et al. Observation of the magnetic flux and three-dimensional structure of skyrmion lattices by electron holography. *Nat. Nanotechnol.* **9**, 337–342 (2014).
6. Braun, H.-B. Topological effects in nanomagnetism: from superparamagnetism to chiral quantum solitons. *Adv. Phys.* **61**, 1–116 (2012).
7. Coronado, E. Molecular magnetism: from chemical design to spin control in molecules, materials and devices. *Nat. Rev. Mater.* **5**, 87–104 (2020).
8. Nagaosa, N. & Tokura, Y. Topological properties and dynamics of magnetic skyrmions. *Nat. Nanotechnol.* **8**, 899–911 (2013).
9. Mühlbauer, S. et al. Skyrmion lattice in a chiral magnet. *Science* **323**, 915–919 (2009).
10. Shibata, K. et al. Large anisotropic deformation of skyrmions in strained crystal. *Nat. Nanotechnol.* **10**, 589–592 (2015).
11. Donnelly, C. et al. Three-dimensional magnetization structures revealed with X-ray vector nanotomography. *Nature* **547**, 328–331 (2017).
12. Rana, A. et al. Direct observation of 3D topological spin textures and their interactions using soft X-ray vector ptychography. Preprint at https://doi.org/10.48550/arXiv.2104.12933 (2021).
13. Bode, M. et al. Atomic spin structure of antiferromagnetic domain walls. *Nat. Mater.* **5**, 477–481 (2006).
14. McVitie, S. & Cushley, M. Quantitative Fresnel Lorentz microscopy and the transport of intensity equation. *Ultramicroscopy* **106**, 423–431 (2006).
15. Lichte, H. Performance limits of electron holography. *Ultramicroscopy* **108**, 256–262 (2008).
16. McVitie, S. et al. Aberration corrected Lorentz scanning transmission electron microscopy. *Ultramicroscopy* **152**, 57–62 (2015).
17. Tate, M. W. et al. High dynamic range pixel array detector for scanning transmission electron microscopy. *Microsc. Microanal.* **22**, 237–249 (2016).
18. Ophus, C. Four-dimensional scanning transmission electron microscopy (4D-STEM): from scanning nanodiffraction to ptychography and beyond. *Microsc. Microanal.* **25**, 563–582 (2019).
19. Chapman, J., Batson, P., Waddell, E. & Ferrier, R. The direct determination of magnetic domain wall profiles by differential phase contrast electron microscopy. *Ultramicroscopy* **3**, 203–214 (1978).
20. Nguyen, K. X. et al. Disentangling magnetic and grain contrast in polycrystalline FeGe thin films using four-dimensional Lorentz scanning transmission electron microscopy. *Phys. Rev. Appl.* **17**, 034066 (2022).
21. Aharonov, Y. & Bohm, D. Significance of electromagnetic potentials in the quantum theory. *Phys. Rev.* **115**, 485–491 (1959).
22. Yu, X. Z. et al. Near room-temperature formation of a skyrmion crystal in thin-films of the helimagnet FeGe. *Nat. Mater.* **10**, 106–109 (2011).
23. Kovács, A. et al. Mapping the magnetization fine structure of a lattice of Bloch-type skyrmions in an FeGe thin film. *Appl. Phys. Lett.* **111**, 192410 (2017).
24. McGrouther, D. et al. Internal structure of hexagonal skyrmion lattices in cubic helimagnets. *New J. Phys.* **18**, 095004 (2016).
25. Mermin, N. D. The topological theory of defects in ordered media. *Rev. Mod. Phys.* **51**, 591–648 (1979).
26. Milnor, J. W. *Topology From the Differentiable Viewpoint* (Press Of Virginia, 1965).
27. Chen, Z. et al. Mixed-state electron ptychography enables sub-angstrom resolution imaging with picometer precision at low dose. *Nat. Commun.* **11**, 2994 (2020).
28. Suzuki, T. et al. Improvement of the accuracy of phase observation by modification of phase-shifting electron holography. *Ultramicroscopy* **118**, 21–25 (2012).
29. Boureau, V. et al. High-sensitivity mapping of magnetic induction fields with nanometer-scale resolution: comparison of off-axis electron holography and pixelated differential phase contrast. *J. Phys. D: Appl. Phys.* **54**, 085001 (2020).
30. Close, R., Chen, Z., Shibata, N. & Findlay, S. D. Towards quantitative, atomic-resolution reconstruction of the electrostatic potential via differential phase contrast using electrons. *Ultramicroscopy* **159**, 124–137 (2015).
31. Isaacson, M. Electron beam induced damage of organic solids: implications for analytical electron microscopy. *Ultramicroscopy* **4**, 193–199 (1979).

32. Thibault, P. & Menzel, A. Reconstructing state mixtures from diffraction measurements. *Nature* **494**, 68–71 (2013).
33. Chen, Z. et al. Electron ptychography achieves atomic-resolution limits set by lattice vibrations. *Science* **372**, 826–831 (2021).

Methods

Experiments

The FeGe single crystals were grown by a chemical vapour transport method[34]. A thin-plate transmission electron microscopy sample along the [110] axis was fabricated using a lift-out method by a focused-ion beam (Thermo Fisher, Strata 400) with 2 kV Ga^+ beam energy for the last thinning step to reduce sample damage. LSTEM was carried out in a field-free mode on a Thermo Fisher Themis Titan microscope operating at 300 keV with a probe forming a semi-angle of 0.23 mrad. The diffraction-limited probe resolution is ~5 nm. The 4D-LSTEM datasets were acquired using an exposure time of 1 ms and beam current of 23 pA employing a high-dynamic-range EMPAD. The scan step sizes of the datasets varied from 1.6 to 2.3 nm. One dataset contains 256 × 256 diffraction patterns and took ~2 min to acquire. The camera length used for the acquisition of the 4D datasets was 19 m with the centre disk covering 17.5 pixels of the detector in radius. Low-temperature electron microscopy was achieved by using a dual-axis Gatan liquid nitrogen holder (Gatan model 613). The external magnetic field, vertical to the sample, was applied using the field from one electromagnetic lens (objective) of the microscope with a controlled current. The lens current versus magnetic field was calibrated using a homemade Hall probe chip mounted on a Protochips biasing holder. The relative rotation between the scanning and diffraction directions at each objective lens current was calibrated using a standard carbon grating sample with gold particles. The probe-position-dependent diffraction shift was carefully minimized by adjusting the scan/descan pivot points and diffraction focus, and no visible shift can be seen at the magnification used for our 4D data acquisition.

LEP

Following the conventional ptychography[35], LEP uses scanning diffraction patterns to reconstruct the complex sample transmission function and the incident probe function under multiplicative approximation[36]. The projected magnetic vector potential can be obtained from the phase of the transmission function when the electrostatic potential contribution due to sample thickness variation is negligible in local uniform regions. Commonly used wedge-like samples with linear thickness variation adds a linear phase shift and constant offset in the magnetic field. We removed this small contribution from the change in sample thickness by making each component of the magnetic field have zero mean in magnitude. It should be noted that the nonlinear variations in electrostatic potential due to surface roughness or sample curvatures may not be separated from the magnetic signal by such an approach. We estimate the contribution to the magnetic field from the sample-thickness variations in this work by using $\varphi_e(x,y) = \sigma_e V_0 \nabla t(x,y)$, where σ_e is the interaction constant and V_0 is the mean inner potential. The equivalent field from such variation is shown in Supplementary Fig. 1 with a standard deviation smaller than 0.07 T. It is noted that the field from the electrostatic potential does not show similar patterns as the magnetic skyrmions and mostly has long-range random-like features. The quantification of the magnetic field in smaller regions (Figs. 2 and 3c) is negligibly affected by the electrostatic contribution.

A focused-probe illumination setup was chosen for the datasets used in the LEP. We adapted the generalized maximum-likelihood ptychography method initially developed for X-ray ptychography[37,38]. Partial coherence of the probe was modelled using a mixed-state model via the modal decomposition approach[32]. Minor variations in the illumination probe due to the instability of electron optics and scanning system were considered using the orthogonal probe relaxation approach[39]. Ptychography from experimental data reaches good convergence after a few hundred iterations. One typical example is shown in Supplementary Fig. 2 with both error evolution and shape of the reconstructed probe modes. The pixel size of the reconstructed phase image is 1.18 nm with the maximum scattering angle of 0.843 mrad in the diffraction patterns.

Ptychographic reconstruction starts from an ideal focused probe as the initial probe and a random phase with a constant magnitude as the initial object. The reconstruction from different initial guesses shows very small numerical differences with a standard deviation of ~0.02 rad (a phase error of less than 1% of the maximum) corresponding to a magnetic field of ~13 mT, which is smaller than the field magnitude of 20 mT at ~1.2 nm away from the singular points near the cores or boundaries of skyrmions (Supplementary Fig. 3). The phase uncertainty mainly comes from the uncertainty of the probe position due to sample vibration and drift under the cryogenic imaging condition. Simulations without sample drift show a phase error more than two orders smaller (~0.0006 rad) using similar imaging parameters (Supplementary Fig. 4). The reconstruction time is roughly linearly dependent on the number of diffraction patterns. Each iteration on a good graphics processing unit card (for example, NVIDIA A6000) takes less than 1 s using 124 × 124 diffraction patterns with each binned down to 64 × 64 pixels, which means that the reconstruction (for example, Supplementary Fig. 3a) can converge within 10 min.

The magnetic induction field was calculated via a first-order gradient of the phase reconstructed from ptychography. A light Gaussian smoothing with a standard deviation of two pixels, that is, 2.36 nm, was applied for a better display (Figs. 1–3), but no smoothing was applied when the precision of the phase or field was estimated (Fig. 4).

Data analysis

Sample thickness t was measured using the Beer's law[40], that is, $\ln\left(\frac{I_t}{I_0}\right) = t/\lambda_{el}$, where I_0 is the intensity of the centre disk of the diffraction pattern, I_t is the incident-beam intensity measured from vacuum and λ_{el} is the elastic mean free path. The elastic mean free path of FeGe for 300 keV electrons was estimated to be 46.4 nm using Wentzel potentials as the atomic-scattering potentials[40], which have been proven to be sufficient for thickness measurements[41]. We also verified the thickness from diffraction and elastic mean free path data by using the electron energy loss spectroscopy method. For this method, the collection angle is 44.9 mrad and the probe-forming semi-angle is 30.0 mrad, and thus, the inelastic mean free path of FeGe is estimated to be 91.9 nm (ref. [42]). As shown in Supplementary Fig. 5, good agreement within 10% is achieved between these two methods. The precision was measured from the fluctuations in phase or magnetic field by estimating the deviation from a local smoothing function. To reduce any bias from the fitting parameters, we used the autocorrelation function of the residual instead of the direct residual[43]. One example of both phase and field is shown in Supplementary Fig. 6. For the simulations in Fig. 4 and Extended Data Figs. 5 and 6, diffraction patterns were calculated under multiplicative approximation[36] from the model phase images formed from 2D Gaussian functions. The spatial resolution (Fig. 4a) was obtained from the radial distribution function of the Fourier intensity of phase images for both integrated centre of mass (iCoM) or ptychography. The threshold frequency above the noise level in the radial distribution function, multiplied by 1.22, is chosen as the resolution to match the Rayleigh criterion.

Determining magnetic field precision

The precision of the experimental magnetic induction field from LEP in terms of deflection angle is 0.6 μrad, corresponding to a magnetic field of 0.01 T from a 100-nm-thick specimen with 300 keV electrons. This should be considered as a conservative upper limit similar to the case in phase measurements. The precision from vacuum without any sample is ~0.17 μrad estimated from direct CoM and is about three times better (Supplementary Fig. 7). The saturation field M_S in the skyrmion lattice state, measured by averaging the local maxima around a skyrmion core, is 0.32 ± 0.02 T at 94 K and 0.16 ± 0.02 T at 240 K (Supplementary Fig. 8). Both are ~80% of the values predicted from an ideal cylindrical skyrmion model[44], but agrees very well with previous

reported results from electron holography[44]. The chiral surface twist has been considered as a possible origin for such discrepancy[44]. We also notice that the fluctuations in the measured phase and magnetic field images may be larger than that can be caused from experimental uncertainties such as sample surface roughness or scanning drift during imaging. Therefore, there may be intrinsic spin fluctuations in the skyrmion states caused by local perturbations such as strain variation[10] or thermal fluctuations[45].

Micromagnetic simulations

Micromagnetic simulations were carried out using the MuMax3.9 software[46]. The unit cell size is $1 \times 1 \times 3$ nm^3 and the total simulation volume is $900 \times 900 \times 30$ nm^3. The micromagnetic energy density includes the exchange energy ($A_{ex} = 1.35 \times 10^{-12}$ J m^{-1}), Dzyaloshinskii–Moriya interaction (0.242×10^{-3} J m^{-2}) and Zeeman energy ($B_{ext} = 0.13$ T). The saturation magnetization is 290 kA m^{-1}.

Data availability

The full raw experimental data is available via Zenodo at https://doi.org/10.5281/zenodo.6684163 (ref. [47]).

Code availability

The source code for LEP is available via Zenodo at https://doi.org/10.5281/zenodo.4659690 (ref. [48]).

References

34. Stolt, M. J., Sigelko, X., Mathur, N. & Jin, S. Chemical pressure stabilization of the cubic B20 structure in skyrmion hosting $Fe_{1-x}Co_xGe$ alloys. *Chem. Mater.* **30**, 1146–1154 (2018).
35. Maiden, A. M. & Rodenburg, J. M. An improved ptychographical phase retrieval algorithm for diffractive imaging. *Ultramicroscopy* **109**, 1256–1262 (2009).
36. Rodenburg, J. M. & Bates, R. H. T. The theory of super-resolution electron microscopy via Wigner-distribution deconvolution. *Philos. Trans. R Soc. A* **339**, 521–553 (1992).
37. Thibault, P. & Guizar-Sicairos, M. Maximum-likelihood refinement for coherent diffractive imaging. *New J. Phys.* **14**, 063004 (2012).
38. Odstrcil, M., Menzel, A. & Guizar-Sicairos, M. Iterative least-squares solver for generalized maximum-likelihood ptychography. *Opt. Express* **26**, 3108–3123 (2018).
39. Odstrcil, M. et al. Ptychographic coherent diffractive imaging with orthogonal probe relaxation. *Opt. Express* **24**, 8360–8369 (2016).
40. Reimer, L. *Transmission Electron Microscopy* (Springer, 1989).
41. Lubk, A. et al. Nanoscale three-dimensional reconstruction of elastic and inelastic mean free path lengths by electron holographic tomography. *Appl. Phys. Lett.* **105**, 173101 (2014).
42. Egerton, R. F. & Cheng, S. C. Measurement of local thickness by electron energy-loss spectroscopy. *Ultramicroscopy* **21**, 231–244 (1987).
43. Bechhoefer, J. Curve fits in the presence of random and systematic error. *Am. J. Phys.* **68**, 424–429 (2000).
44. Song, D. et al. Quantification of magnetic surface and edge states in an FeGe nanostripe by off-axis electron holography. *Phys. Rev. Lett.* **120**, 167204 (2018).
45. Mochizuki, M. et al. Thermally driven ratchet motion of a skyrmion microcrystal and topological magnon Hall effect. *Nat. Mater.* **13**, 241–246 (2014).
46. Vansteenkiste, A. et al. The design and verification of MuMax3. *AIP Adv.* **4**, 107133 (2014).
47. Chen, Z. & Muller, D. A. Datasets for Lorentz electron ptychography for imaging magnetic textures beyond the diffraction limit. *Zenodo* https://doi.org/10.5281/zenodo.6684163 (2022).
48. Chen, Z., Jiang, Y., Muller, D. A. & Odstrcil, M. PtychoShelves_EM, source code for multislice electron ptychography. *Zenodo* https://doi.org/10.5281/zenodo.4659690 (2021).

Acknowledgements

This work is supported by the DARPA TEE-D18AC00009. Z.C. was partly supported by the PARADIM Materials Innovation Platform in-house program by NSF grant DMR-2039380. M.J.S. and S.J. were supported by NSF ECCS-1609585. This work made use of the Cornell Center for Materials Research facility supported by NSF grant DMR-1719875.

Author contributions

Z.C., D.A.M., G.D.F. and D.C.R. conceived the project. Z.C. performed the experiments and data analysis under the supervision of D.A.M. E.T. carried out the micromagnetic simulations. Y.J. contributed to the LEP. E.T. and K.X.N. performed the magnetic field calibration of the electron microscope. M.J.S. synthesized the FeGe single crystal under the supervision of S.J. Z.C. wrote the draft with revisions from D.A.M. All the authors discussed the results and implications throughout the investigation and have given approval to the final version of the manuscript.

Competing interests

Cornell University has licensed the EMPAD hardware to Thermo Scientific (D.M. and K.X.N. each receives 4.4% of the license fee).

Additional information

Extended data is available for this paper at https://doi.org/10.1038/s41565-022-01224-y.

Supplementary information The online version contains supplementary material available at https://doi.org/10.1038/s41565-022-01224-y.

Correspondence and requests for materials should be addressed to Zhen Chen or David A. Muller.

Peer review information *Nature Nanotechnology* thanks Jianwei (John) Miao and the other, anonymous, reviewer(s) for their contribution to the peer review of this work.

https://doi.org/10.1038/s41565-022-01224-y

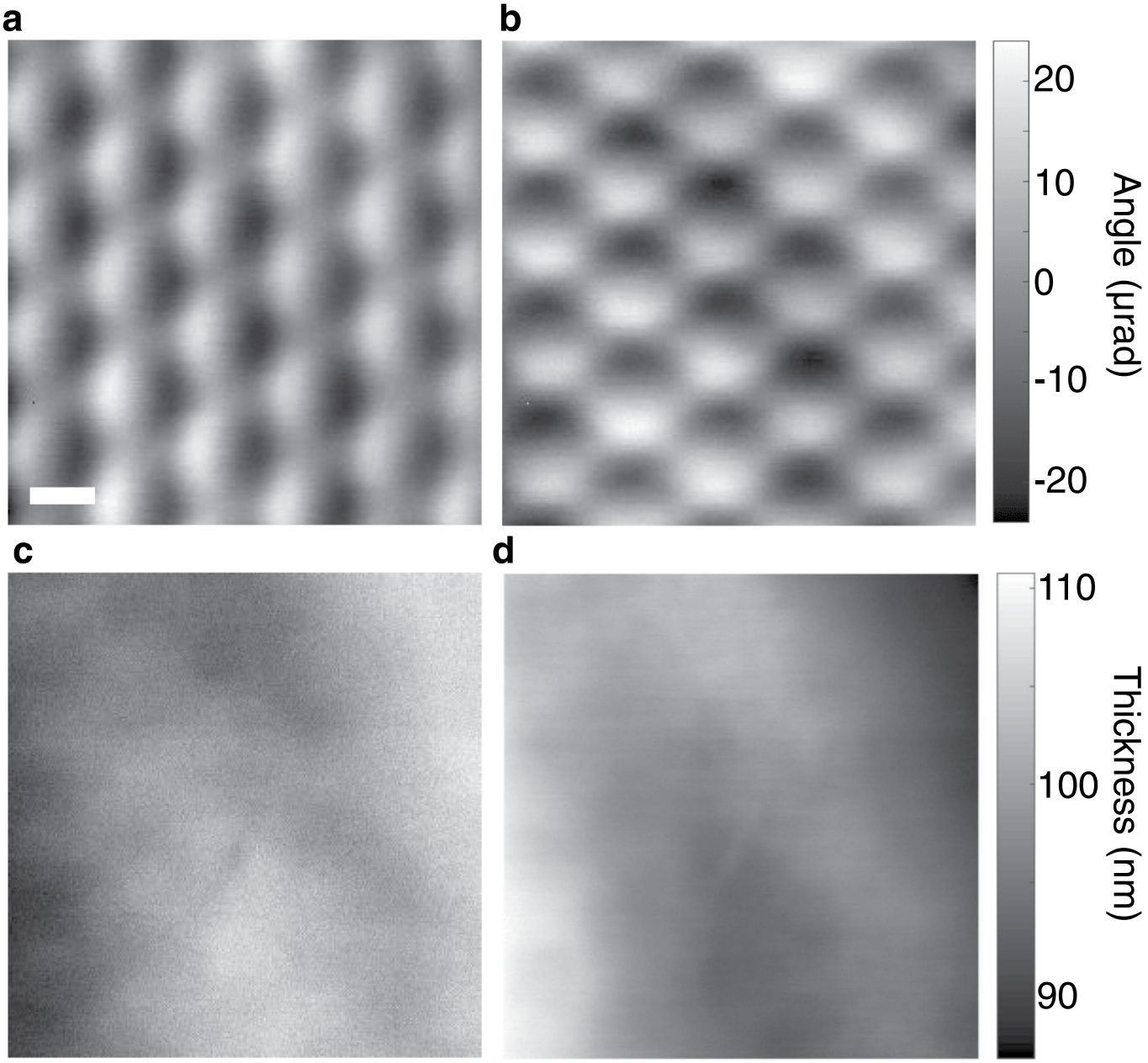

Extended Data Fig. 1 | Synthesized image modes from the 4D LSTEM dataset used in Fig. 1. a, Center-of-mass (CoM) along horizontal direction (x-axis) ; **b**, CoM along vertical direction (y-axis); **c**, Annular dark-field (ADF) image; **d**, Thickness determined from the diffraction. Scale bar is 50 nm.

https://doi.org/10.1038/s41565-022-01224-y

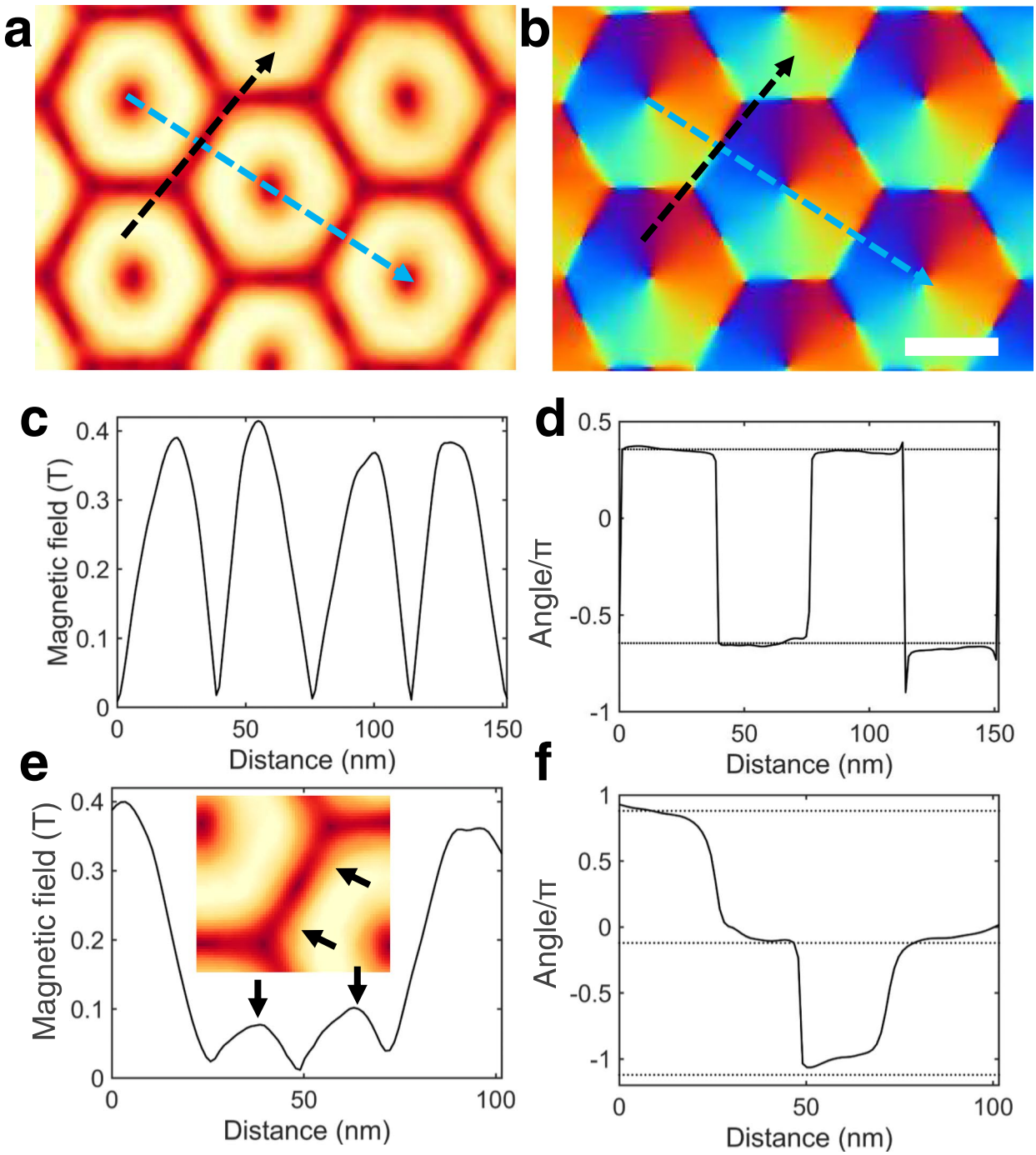

Extended Data Fig. 2 | Discontinuity near skyrmion boundaries. **a, b**, Magnitude and direction of lateral magnetic field of skyrmion lattice in FeGe, respectively. Scale bar is 50 nm. **c, d**, Magnitude (**c**) and direction (**d**) of the magnetic field along the blue dashed line marked on (**a**) and (**b**). **e & f**, Magnitude (**e**) and direction (**f**) of the magnetic field along the black dashed line marked on (**a**) and (**b**). In order to show the reversal of the magnetic field direction across the boundaries, the line for (**d**) and (**f**) is slightly away the skyrmion boundary. The inset in (e) is a cropped region of (a) with arrows indicating the local maxima along the skyrmion boundary.

https://doi.org/10.1038/s41565-022-01224-y

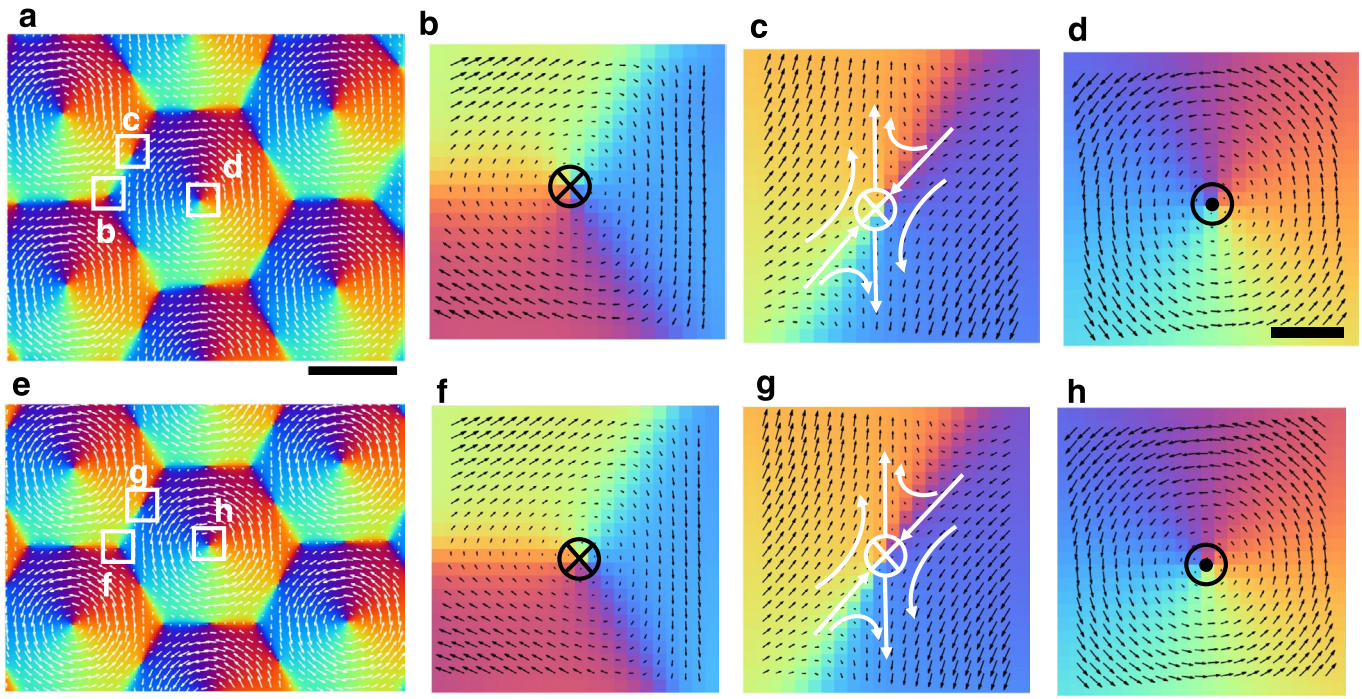

Extended Data Fig. 3 | Comparison of measured and simulated magnetization of skyrmion lattice. a, Experimental measurements of magnetization vector map; **b**-**d**, Enlarged magnetization vector maps near the singular points labeled on (**a**). **e**-**h**, Micromagnetic simulations of magnetization of skyrmions lattice and singular points. Scale bar for (**a**) and (**e**) is 50 nm, for (**b**)-(**d**) and (**f**)-(**h**) is 2 nm.

https://doi.org/10.1038/s41565-022-01224-y

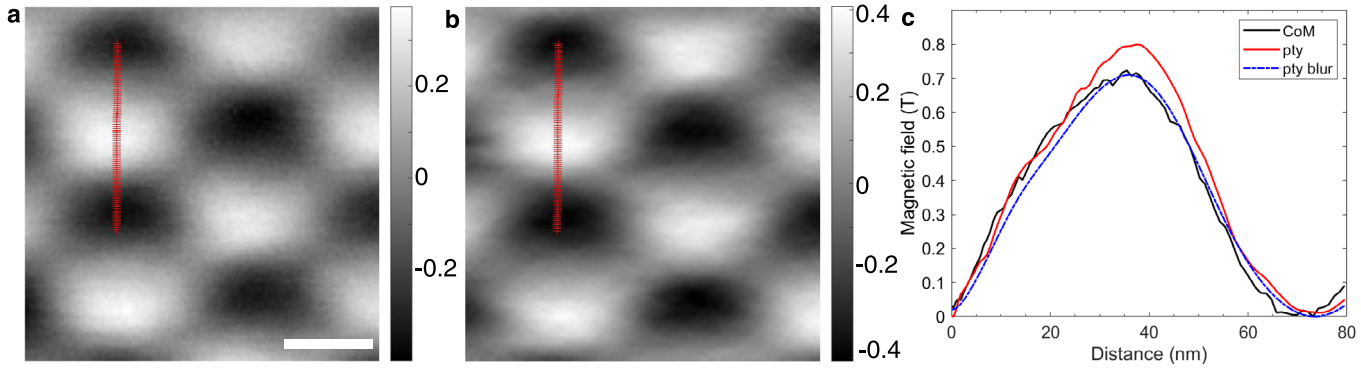

Extended Data Fig. 4 | Resolution improvements of ptychography compared to center-of-mass (CoM). Magnetic field (B_x) from CoM (**a**) and ptychography (**b**). **c**, Line profiles from the position marked by the red line on (**a**) and (**b**). The profile from CoM has a further broadening of 12.4 nm (Gaussian, FWHM) compared to that from ptychography (pty_blur).

https://doi.org/10.1038/s41565-022-01224-y

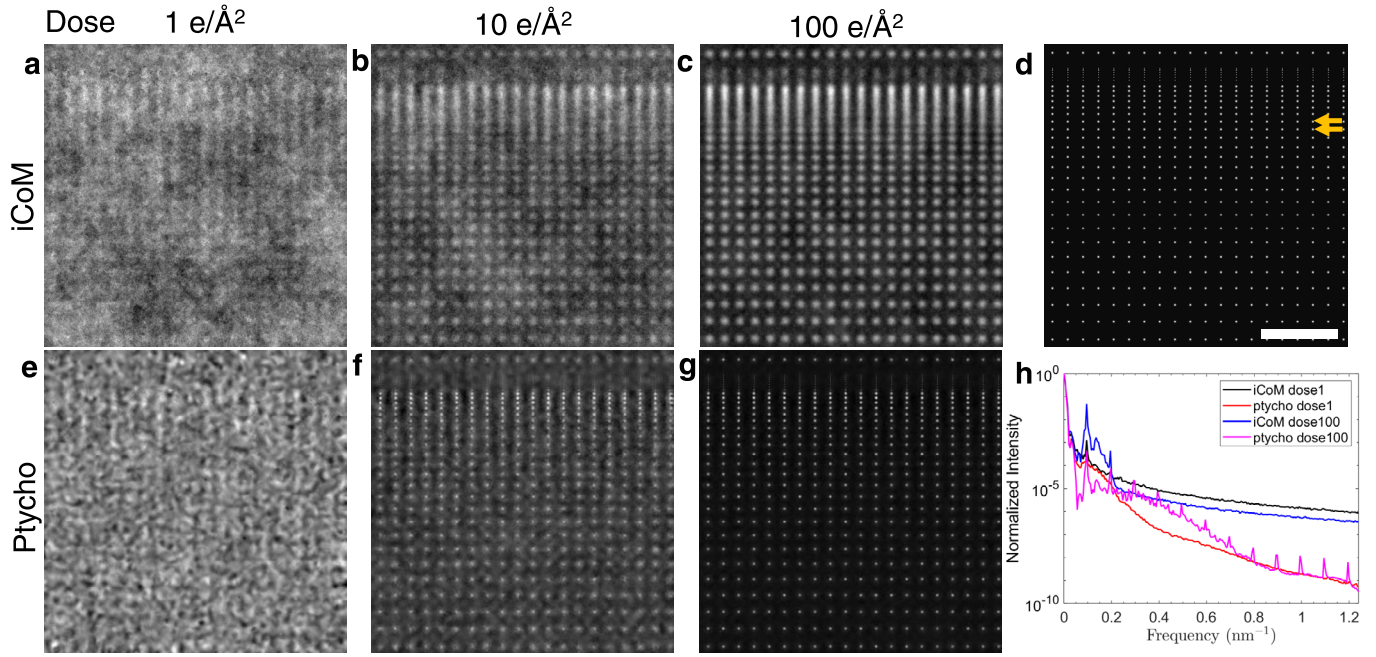

Extended Data Fig. 5 | Simulations for sub-nanometer spatial resolution of ptychography. a–**c**, Phase images from iCoM and **e**–**g**, from ptychography at different doses; **d**, The model phase structure used to generate diffraction patterns; **h**, Radial distribution function of the Fourier intensity of phase images in (**a**), (**c**), (**e**), (**g**). The model structure contains varying peak distances vertically and the arrows on (**d**) mark two rows with the distance of 5.2 nm. Scale bar is 50 nm.

https://doi.org/10.1038/s41565-022-01224-y

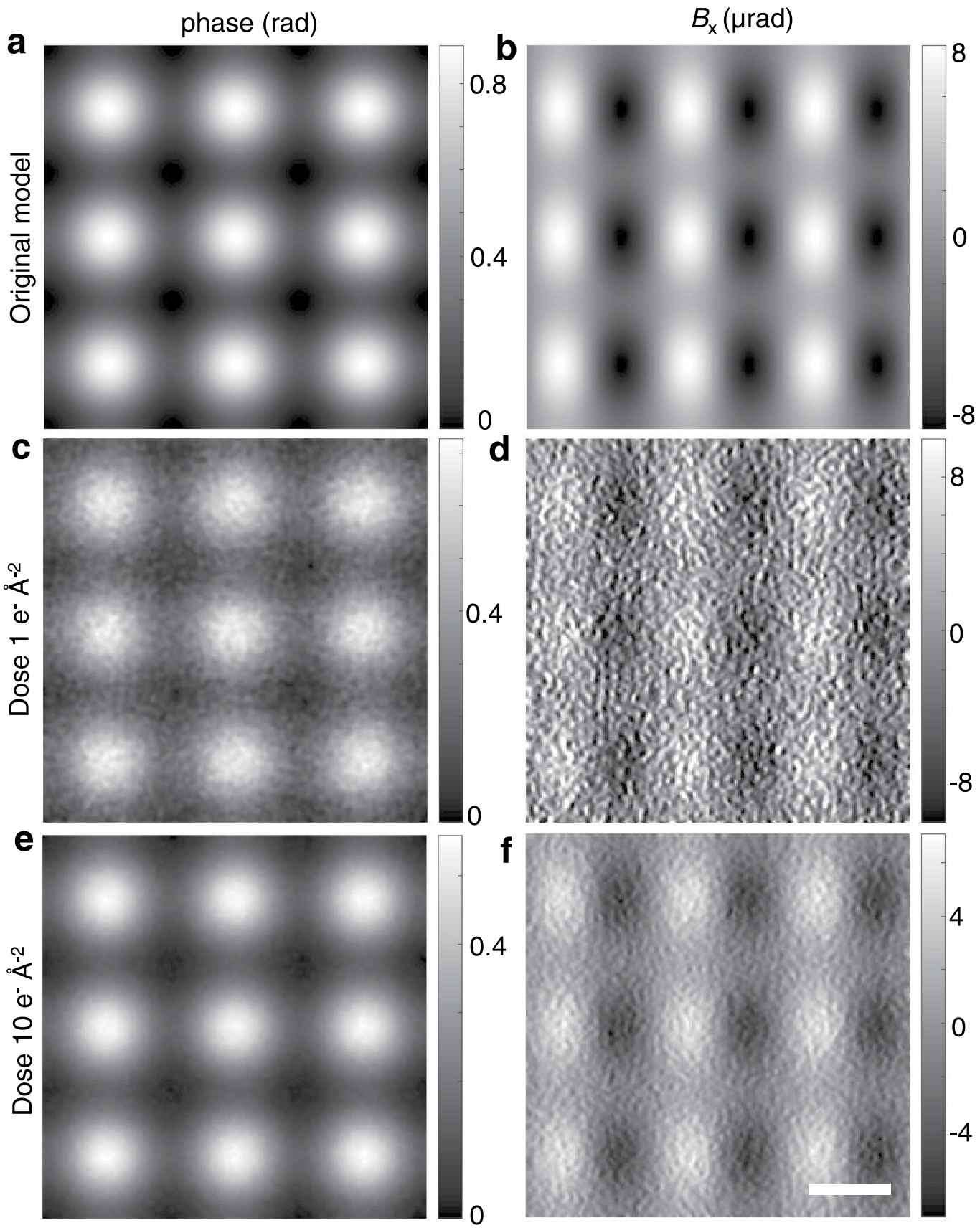

Extended Data Fig. 6 | Model phase image for ptychography simulations. **a**, Original phase image for ptychography simulations generated from arrays of two-dimensional Gaussian functions; **b**, Field strength along horizontal direction from (**a**). **c, d**, Phase and field retrieved from ptychography with an illuminating dose of 1 e^- Å^{-2}, respectively. **e, f**, Phase and field retrieved from ptychography with an illuminating dose of 10 e^- Å^{-2}, respectively. Scale bar is 30 nm.